

Article

Destabilization of the $\text{LiBH}_4\text{--NaBH}_4$ Eutectic Mixture through Pore Confinement for Hydrogen Storage

Filippo Peru^{1,2}, Seyedhosein Payandeh^{3,4} , Torben R. Jensen³ , Georgia Charalambopoulou¹ 
and Theodore Steriotis^{1,*} ¹ National Centre for Scientific Research “Demokritos”, Ag. Paraskevi Attikis, 15341 Athens, Greece² Inorganic Chemistry Laboratory, Department of Chemistry, National and Kapodistrian University of Athens, Panepistimiopolis Zografou, 15771 Athens, Greece³ Interdisciplinary Nanoscience Center (iNANO) and Department of Chemistry, University of Aarhus, Langelandsgade 140, DK-8000 Aarhus C, Denmark⁴ Electronics & Electrification (BEB-S) Department, FEV Group, Neuenhofstraße 181, 52078 Aachen, Germany

* Correspondence: t.steriotis@inn.demokritos.gr

Abstract: Both LiBH_4 and NaBH_4 are well known for having high hydrogen contents, but also high decomposition temperatures and slow hydrogen absorption–desorption kinetics, preventing their use for hydrogen storage applications. The low melting temperature (219 °C) of their eutectic mixture 0.71 $\text{LiBH}_4\text{--}0.29 \text{NaBH}_4$ allowed the synthesis of a new composite material through the melt infiltration of the hydrides into the ~5 nm diameter pores of a CMK-3 type carbon. A composite of 0.71 $\text{LiBH}_4\text{--}0.29 \text{NaBH}_4$ and non-porous graphitic carbon discs was also prepared by similar methods for comparison. Both composites showed improved kinetics and a partial reversibility of the dehydrogenation/rehydrogenation reactions. However, the best results were observed for the CMK-3 nanoconfined hydrides; a consistent uptake of about 3.5 wt.% H_2 was recorded after five hydrogenation/dehydrogenation cycles for an otherwise non-reversible system. The improved hydrogen release kinetics are attributed to carbon–hydride surface interactions rather than nanoconfinement, while enhanced heat transfer due to the carbon support may also play a role. Likewise, the carbon–hydride contact proved beneficial in terms of reversibility, without, however, ruling out the potential positive effect of pore confinement.

Keywords: hydrogen storage; complex hydrides; nanoconfinement; borohydrides; porous carbons



Citation: Peru, F.; Payandeh, S.; Jensen, T.R.; Charalambopoulou, G.; Steriotis, T. Destabilization of the $\text{LiBH}_4\text{--NaBH}_4$ Eutectic Mixture through Pore Confinement for Hydrogen Storage. *Inorganics* **2023**, *11*, 128. <https://doi.org/10.3390/inorganics11030128>

Academic Editor: Maurizio Peruzzini

Received: 26 January 2023

Revised: 9 March 2023

Accepted: 16 March 2023

Published: 18 March 2023



Copyright: © 2023 by the authors. Licensee MDPI, Basel, Switzerland. This article is an open access article distributed under the terms and conditions of the Creative Commons Attribution (CC BY) license (<https://creativecommons.org/licenses/by/4.0/>).

1. Introduction

Climate change and its mitigation is one of the most important challenges that humankind will face in the 21st century. The reduction of greenhouse gas emissions is a fundamental measure in order to reverse the global warming trend, and massive effort is thus directed to moderate the anthropogenic CO_2 production [1,2]. The compelling necessity to divert the energy production and consumption from fossil fuel combustion towards more sustainable renewable sources is clear. Nevertheless, the majority of such renewable sources (such as wind, solar and tidal power) have the major drawback of variability, in several cases in an unpredictable fashion, due to their fluctuating nature. In order to have a reliable and sustainable energy supply, it is necessary to adopt an energy carrier able to accumulate the energy produced through renewable energy sources and provide it when and where it is required. ‘Green’ hydrogen could be such a sustainable energy carrier [3,4] not only for having just water as the byproduct of its combustion reaction, but also due to its high energy density, i.e., 120 MJ kg^{-1} ($33.33 \text{ kWh kg}^{-1}$), which is twice as high as that of the common fuels [5]. This property is particularly interesting especially for mobile applications, where energy must be stored onboard. However, the extremely low density of hydrogen gas is a considerable obstacle for its practical use in common applications. For instance, for storing 5 kg of H_2 (equivalent to a car autonomy of about 500 km) at 200 bar

(typical pressure of commercial hydrogen cylinders), a tank volume of about 340 L would be required [6,7]. H₂ liquefaction at very low temperatures, around 20 K (−253 °C) or pressurization to 700 bar, can reduce the system volume, but then significant amounts of energy are sacrificed (for cooling or pressurization but also due to boil-off), while more advanced and expensive vessels are needed [8]. Cryo-compressed hydrogen storage [9,10] has some significant advantages such as improved gravimetric and volumetric capacities compared with compressed hydrogen, but also reduced boil-off compared with typical liquid H₂ storage systems. In all cases, the required pressure increase or temperature decrease comes along with a significant energy penalty, while serious safety issues emerge [11,12]. A much safer approach, which may avoid the multiple disadvantages of compressed gas storage and operation at very low temperatures, involves the use of solid-state materials with high hydrogen content [13–19]. Among the materials considered as good candidates for low-pressure solid-state hydrogen storage, borohydrides, which are able to release hydrogen simply through their thermal decomposition, have particularly attractive characteristics [16,20–25]. These materials generally have a high gravimetric and volumetric hydrogen density, e.g., LiBH₄ and NaBH₄, whose gravimetric and volumetric capacities are 18.5 and 10.6 wt.% and 121 and 113 kg m^{−3}, respectively [26–28]. However, these materials are highly stable, a property that leads directly to high decomposition temperatures, slow kinetics and in several cases lack of reversibility of the dehydrogenation/hydrogenation reaction [28–34]. Ion substitution and liquefaction can help reduce the temperatures required for the hydrogen release from borohydrides. Both phenomena have been studied on several combinations of such compounds and the most appreciable effects are observed when using eutectic mixtures [35–40].

This work focuses on the study of a LiBH₄–NaBH₄ eutectic composite. The pure LiBH₄ and NaBH₄ are known to melt at 280 °C and 505 °C, respectively, while their main dehydrogenation reactions take place at temperatures higher than 400 °C [35,41,42]. On the other hand, upon mixing LiBH₄ (71 mol%) and NaBH₄ (29 mol%), a eutectic mixture is formed as reported by Dematteis et al. [43]. This mixture has a gravimetric hydrogen content of 15.25 wt.% and a melting temperature of 219 °C, allowing at the same time a drastic destabilization of both compounds and the possibility to melt the hydrides in relatively mild conditions with minimal risk of decomposition. Other approaches that can further destabilize the material, reduce the decomposition temperature and enhance the pertinent kinetics most commonly involve particle size reduction and contact with other materials' surfaces [44,45]. Particle size reduction, in most cases, is achieved through mechanical milling [46,47]. This approach aims to afford particle sizes in the order of nanometers. For such small particles, the surface to volume ratio increases significantly, providing shorter diffusion paths in the solid state and the hydrogen release kinetics are improved significantly. However, the benefits of nanosizing by high-energy ball milling are rapidly reverted by sintering reactions occurring during the hydrogenation/dehydrogenation processes. One way to address this problem is to protect the hydride nanoparticles from agglomeration by confining them in nanosized pores. This approach is particularly facile for molten phases such as low temperature eutectic mixtures and has multiple advantages: (i) solvent free nano-infiltration and (ii) prevention of particle growth and agglomeration due to the encapsulation. In order to have the minimum mass penalty from the confining material, it is necessary to adopt a porous solid with very high pore volume and low density. Carbonaceous materials are ideal for this purpose, since they are in principle chemically inert, they can be synthesized in a wide variety of forms and their pore size can be tuned in order to obtain a good balance between easy infiltration in the host material and optimal particle size of the active guest material. Upon confinement, the hydride nanoparticles and the carbon matrix are bound to proximity, forcing the different components to interact. Beyond nanosizing, the system may also benefit from the intimate contact of the hydride phase with the carbon surface. For instance, the high thermal conductivity of the carbon matrix may facilitate heat transfer and therefore promote de- and re- hydrogenation reactions. Moreover, the carbon–hydride's contact could also trigger surface-induced catalytic

reactions due to the carbon electron affinity on the nanoscale, which can promote a decrease in the hydrogen release energy [44,45,48].

A low melting mixture of LiBH_4 and NaBH_4 confined in porous carbon materials for hydrogen storage purposes has been studied by Javadian et al. [49]. However, the borohydride mixture investigated in that specific work consisted of 0.62 LiBH_4 –0.38 NaBH_4 according to the phase diagram proposed by Adams [50], while the molten borohydrides were infiltrated in a porous carbon aerogel with large mesopores (diameter of ca. 40 nm) and tested with only four cycles of dehydrogenation/rehydrogenation. In the present work, we adopted a more recently reported eutectic composition, 0.71 LiBH_4 –0.29 NaBH_4 , with a higher gravimetric hydrogen content [43] of 15.25 wt.%. Moreover, we used for the first time an ordered mesoporous CMK-3 type carbon as hosting material characterized by much smaller pore sizes (5 nm) with a very narrow distribution, which is ideal for nanoconfinement studies. CMK-3 is a mesoporous carbonaceous material made by nanorods organized in a regular 2D hexagonal pattern and held together by thin carbon strands [51]. The high porosity of the CMK-3 structure results in an overall very high pore volume, a characteristic that allows the confinement of large quantities of hydrides. Here, we compare the properties of (a) LiBH_4 – NaBH_4 /CMK-3, (b) the non-confined (bulk) hydrides and (c) a composite of LiBH_4 – NaBH_4 with a non-porous carbon, namely graphitic carbon discs, in order to analyze the effect of nanoconfinement to the destabilization, kinetics and cyclability of hydrogen release and uptake of the LiBH_4 – NaBH_4 eutectic system.

2. Results

The XRPD measurements of bulk, composite and cycled materials are presented in Figure 1. CMK-3 carbon is amorphous, as revealed by the practically featureless powder diffraction pattern. From the analysis of the XRPD pattern of the bulk 0.71 LiBH_4 –0.29 NaBH_4 (denoted LiNa) obtained after the milling process, it was possible to identify the peaks relative to the two pure borohydrides, LiBH_4 and NaBH_4 , while no intermediate compounds were detected; based on Scherrer analysis of the most intense peaks, an average crystallite size of around 20 nm was calculated for both phases. On the other hand, the XRPD pattern of the CMK-3 infiltrated sample (LiNa/CMK-3) showed only the diffraction peaks of NaBH_4 with low intensity. This pattern suggests that although a small amount of bulk hydride remained outside the pores, the majority of the hydride phase was infiltrated in the porous network, causing a significant overall decrease in the peak intensity in a way that only the strongest peaks of the eutectic mixture were detected; these are the (111), (200) and (220) reflections of NaBH_4 . Nevertheless, even these low intensity NaBH_4 diffraction peaks disappeared after the five dehydrogenation–rehydrogenation cycles (LiNa/CMK-3 five cycles pattern), implying that upon further thermal treatment all the borohydride material is eventually infiltrated in the CMK-3 pores. The situation was somehow different for the non-porous CD composite. CD revealed a graphitic structure, with a broad (002) reflection at $\sim 26^\circ$ coupled with another visible feature at $\sim 43^\circ$; this pertained to the merged (100) and (101) reflections. The LiNa structure was fully visible in the LiNa/CD composite, while several diffraction peaks were still visible, even after the five dehydrogenation–rehydrogenation cycles (LiNa/CD, five cycles).

The presence of a small amount of unconfined hydrides was confirmed by the scanning electron microscope images (Figure 2), also showing that the CMK-3 carbon retained its typical rod-like elongated structure, fully withstanding multiple heat treatments.

Nevertheless, the confirmation that the majority of the hydride phase was successfully confined in the porous carbon scaffold was given by the comparison of the pore properties before and after melt infiltration. N_2 adsorption–desorption isotherms at 77 K (approx. -196°C) were measured for the pure CMK-3 type carbon (Figure 3). The isotherm was of type IV(a) according to the IUPAC classification, with an H_2 (a) hysteresis loop; both are characteristic for CMK-3 materials with mesopores larger than ~ 4 nm and a rather sharp size distribution [52]. Based on this isotherm, a Brunauer–Emmett–Teller (BET) surface

area (S_{BET}) of $1250 \text{ m}^2 \text{ g}^{-1}$, a total pore volume (TPV) of $1.2 \text{ cm}^3 \text{ g}^{-1}$ and an average pore size distribution centered at 4.6 nm were deduced for CMK-3 (Table 1).

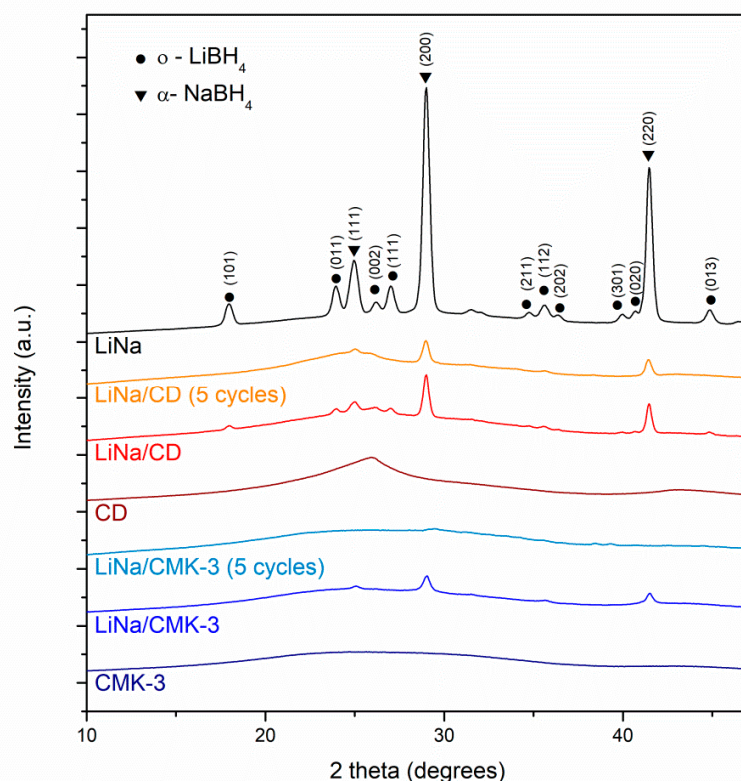


Figure 1. XRPD patterns of pure carbons (CMK-3 and CD), bulk 0.71 LiBH_4 –0.29 NaBH_4 eutectic mixture (LiNa), the carbon/borohydride composites (LiNa/CMK-3 and LiNa/CD) as well as the composites after 5 dehydrogenation and rehydrogenation cycles. The peak labels indicate the following phases: orthorhombic o- LiBH_4 (●), α - NaBH_4 (▼).

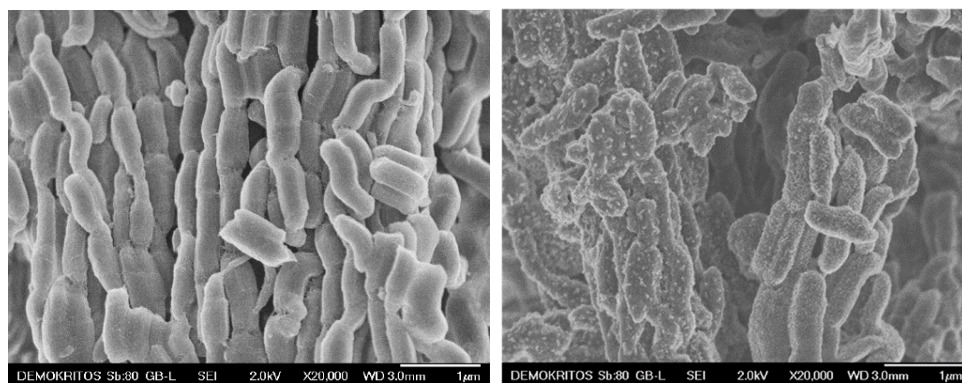


Figure 2. Scanning electron microscope (SEM) pictures showing the typical elongated structure of pure CMK-3 (left) and LiNa/CMK-3 after melt infiltration, with traces of borohydrides on the external surface of the carbon particles (right).

The general shape of the isotherm of LiNa/CMK-3 was the same; nevertheless, the BET area dropped to $170 \text{ m}^2 \text{ g}^{-1}$ and TPV to $0.21 \text{ cm}^3 \text{ g}^{-1}$, while the pore size distribution remained centered at 4.6 nm. This implies that after infiltration a large number of pores were lost (i.e., becoming completely inaccessible to the adsorbate), which strongly suggests that the borohydride molten phase indeed fills the pores and does not form a layer on the pore walls (this would decrease the pore size of the sample). It should be noted that the isotherm of the composite material presented in Figure 3 has been scaled to the mass of

pure carbon (the same holds for the BET and TPV calculations), thus excluding the weight penalty of the non-porous hydride phase. On the other hand, the pristine carbon discs (CDs) showed a clear type-I isotherm, typical for non-porous materials; a BET area of $\sim 30 \text{ m}^2 \text{ g}^{-1}$ was calculated. Both the isotherm shape and the BET area ($\sim 25 \text{ m}^2 \text{ g}^{-1}$) on a carbon basis remained practically unchanged for LiNa/CD (Table 1).

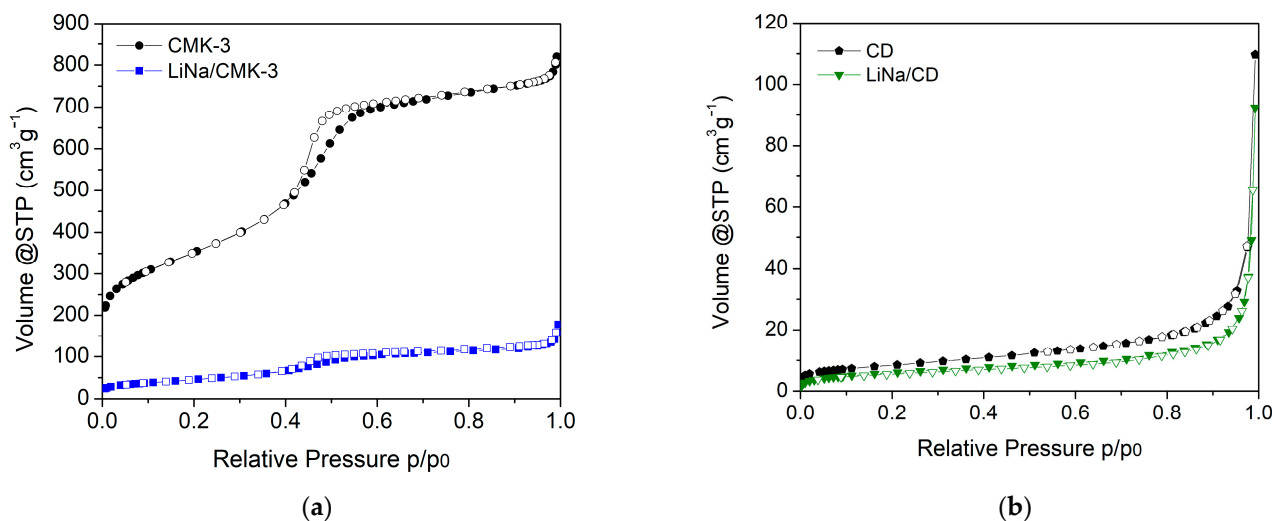


Figure 3. N₂ adsorption/desorption isotherms performed at 77 K (a): on the pure CMK-3 type carbon (black) and on the composite material LiNa/CMK-3 (blue), and (b): on the pure CD (black) and the LiNa/CD samples (green).

Table 1. Surface area (S_{BET}), total pore volume (TPV) and average pore size ($\langle d \rangle$) of pure CMK-3 and carbon discs (CD), as well as their composites with 0.71 LiBH₄–0.29 NaBH₄ (LiNa).

	S_{BET} ($\text{m}^2 \text{ g}^{-1}$)	TPV ($\text{cm}^3 \text{ g}^{-1}$)	$\langle d \rangle$ (nm)
CMK-3	1250	1.2	4.6
LiNa/CMK-3	170	0.21	4.6
CD	~ 30	-	-
LiNa/CD	~ 25	-	-

The temperature programmed desorption-mass spectrometry (TPD-MS) measurement of hydrogen release from bulk LiNa showed that dehydrogenation of the eutectic mixture occurred mostly at an intermediate temperature between that of the two pure components, in accordance with previously reported results for the pure LiBH₄ and NaBH₄ compounds and their mixtures with compositions close to the eutectic one [53]. In more detail, bulk LiNa, after being pre-melted, dehydrogenated in four stages (Figure 4), with a first release at 290 °C (2%), two desorption peaks at about 390 (26%) and 450 °C (39%) and a final decomposition at 490 °C (33%). Based on the shape of the LiNa TPD-MS spectra as compared with the thermal desorption from the pure compounds presented in [54–56], and since the XRPD pattern of LiNa revealed only pure LiBH₄ and NaBH₄, the first three dehydrogenation steps can be directly associated with the decomposition of LiBH₄, while the last one can be attributed to NaBH₄. This observation is very similar to that of Liu et al. [53], who studied a similar mixture of LiBH₄ and NaBH₄ and identified two main decomposition routes: the first (up to ~ 520 °C) involved the release of H₂ followed by the formation of LiH, Li₂B₁₂H₁₂ and B; the second, at higher temperatures, involved the release of H₂ together with the formation of Na and B.

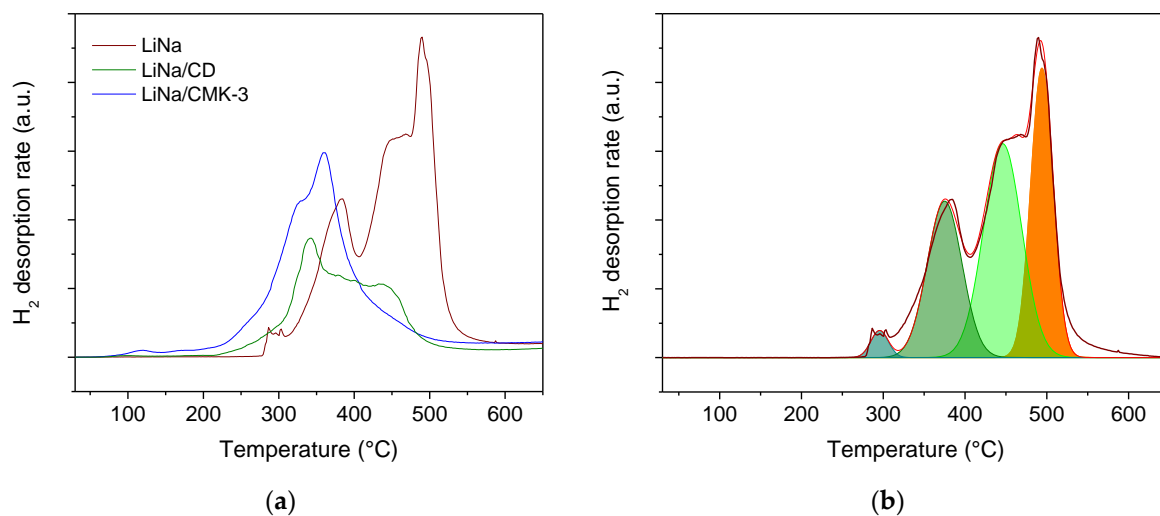
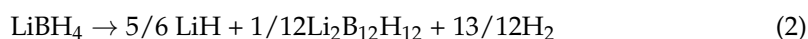


Figure 4. (a): Temperature programmed desorption coupled with mass spectrometry (TPD/MS, $m/e = 2$) results for LiNa (dark red), LiNa/CD (green), LiNa/CMK-3 (blue). (b): Deconvolution of the bulk LiNa TPD signal highlighting the different H₂ release reactions. The first three (green) peaks are attributed to the LiBH₄ decomposition, covering, respectively, the 2%, 26% and 39% of the total H₂ released, while the orange peak is related to the NaBH₄ decomposition (33% of the total H₂ released).

The LiNa/CMK-3 composite released hydrogen in a similar manner to the bulk LiNa and with a similar ratio between the signal intensities. However, the different reaction steps occurred at much lower temperatures and in a shorter temperature range and were somehow merged together, with the main peaks located at 325 and 360 °C, highlighting the contribution from the carbon surface. The substrate's active role in lowering the dehydrogenation temperatures of LiNa was also evident in the behavior of LiNa/CD, which mostly decomposed at 340 and 440 °C. In the latter case, it can be noticed that despite the absence of nanoconfinement, the carbon matrix still played a role in the material destabilization, albeit with less intensity, probably due to the lower surface area of the carbon discs. In all samples, only hydrogen was detected among the gases analyzed.

The hydrogen release and uptake were further investigated for the three samples using a custom-made manometric device (Sieverts apparatus) and a series of dehydrogenation/rehydrogenation cycles (Figure 5). Excessive heating (temperatures higher than 650 °C) led to complete decomposition of NaBH₄ with the precipitation of Na, B and the evolution of H₂ (NaBH₄ → Na + B + 2H₂) [53,57]. Without the aid of catalysts/additives [58–60], this process is highly irreversible and, for this reason, it was decided to limit the cycling experiments to 450 °C and only actually study the decomposition of LiBH₄ (in the presence of NaBH₄). The decomposition of LiBH₄ went through a complex mechanism that can be represented by two main reactions [53,61,62]:



This explains the drastic reduction of hydrogen released between the first and second dehydrogenation cycle for all samples. Due to the stability of Li₂B₁₂H₁₂ closo-borane, we assumed that only the first reaction was reversible and, based on the amount of hydrogen released during the manometric experiments, it can be deduced that it occurred in a percentage of around 60–70% of the LiBH₄ decomposition. It should be noted that attempts to hydrogenate Li₂B₁₂H₁₂-10 LiH composites, e.g., at $p(\text{H}_2) = 970$ bar and $T = 400$ °C for 48 h, did not reveal any formation of LiBH₄ or other compounds [63].

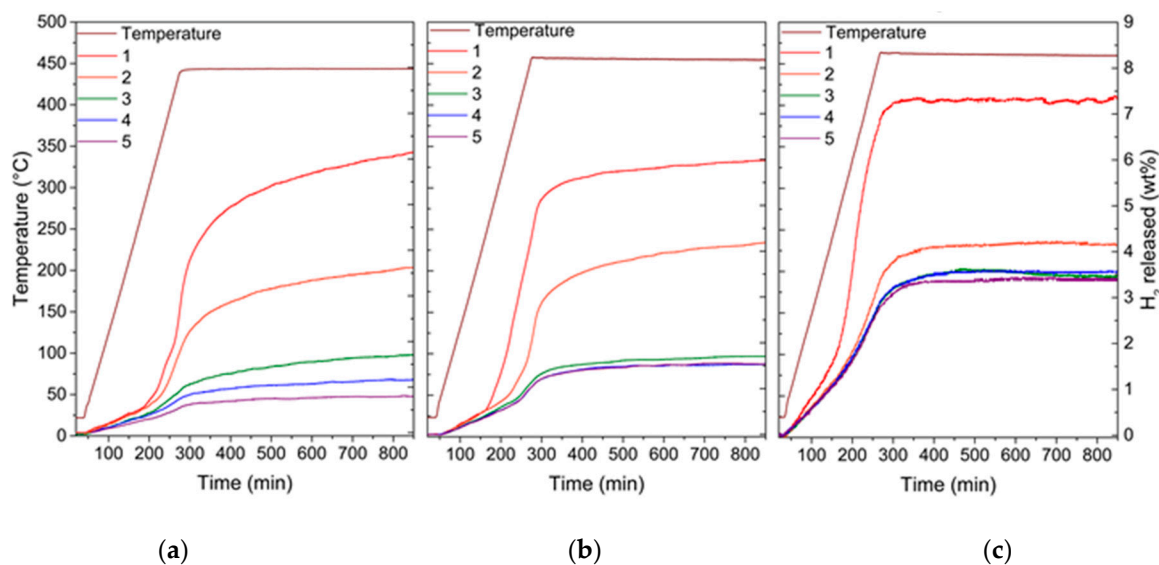


Figure 5. Kinetics and quantitative measurement of hydrogen release and uptake was investigated using a manometric method (Sieverts apparatus). From left to right: (a) LiNa, (b) LiNa/CD and (c) LiNa/CMK-3.

In more detail, the bulk LiNa released about 6.2 wt.% of H_2 , an amount that dropped to 3.6 wt.% already at the second dehydrogenation step and continued to decrease at each cycle until it reached about 0.8 wt.% of H_2 at the fifth hydrogenation–dehydrogenation cycle, suggesting strong deactivation of the system (Figure 5a). It is also important to note that the dehydrogenation kinetics were extremely slow, and during the first cycles the system was far from equilibrium even after 800 min. Taking into account only the mass of the active materials in the hydrogen sorption reaction, i.e., that of $LiBH_4$ and $NaBH_4$ and excluding the carbon, the LiNa/CD composite had a similar behavior with the bulk during the first three cycles, i.e., it released about 6 wt.% of H_2 at the first, 4.2 wt.% of H_2 at the second and 1.7 wt.% during the third cycle. Nevertheless, the sample reached a stable value of around 1.5 wt.% of H_2 for the last three cycles (Figure 5b). In this case, the desorption kinetics were significantly faster compared with the bulk, but still quite slow.

The LiNa/CMK-3 composite, on the other hand, released in a very fast manner (equilibrium reached at around 300 min) about 7.3 wt.% of H_2 in the first cycle, which dropped to 4.2 wt.% in the second dehydrogenation step, but stabilized around 3.5 wt.% for cycles three–five, revealing that at least a part of the infiltrated material retained its reversibility (Figure 5c). The increased release during the first cycle can be attributed to partial decomposition of $NaBH_4$ below 450 °C. This kinetic enhancement was probably due to nanoconfinement, and was also detected in our TPD measurements [64]. However, the decomposed $NaBH_4$, could not be re-hydrogenated and the second cycle finally showed a similar release with the bulk and the LiNa/CD samples. On the other hand, contrary to the CDs, the nanoconfinement in CMK-3 provided more protection, and therefore a higher degree of reversibility, probably by minimizing the formation of closo-boranes.

The derivatives of the kinetic desorption curves of Figure 5 measured with a manometric (Sieverts) approach also reveal some interesting details and are presented in Figure 6 for the first and third cycle. The ramp rates between TPD and cycling experiments were quite different; however, the dehydrogenation curve of bulk LiNa also showed different dehydrogenation events during the first decomposition. Probably due to the much lower amount of hydrogen released, for the third dehydrogenation the signals merged in a broad one in an average position. Additionally, again in accordance with the TPD-MS results, the derivative curve of the first dehydrogenation curve of the composite LiNa/CMK-3 appeared much earlier than the bulk, showing the contribution of the carbon. This, however, seemed to disappear upon cycling and the derivative of the third cycle showed that the

main hydrogen desorption occurred later, similarly to that of the bulk. As expected, the LiNa/CD composite showed an intermediate behavior.

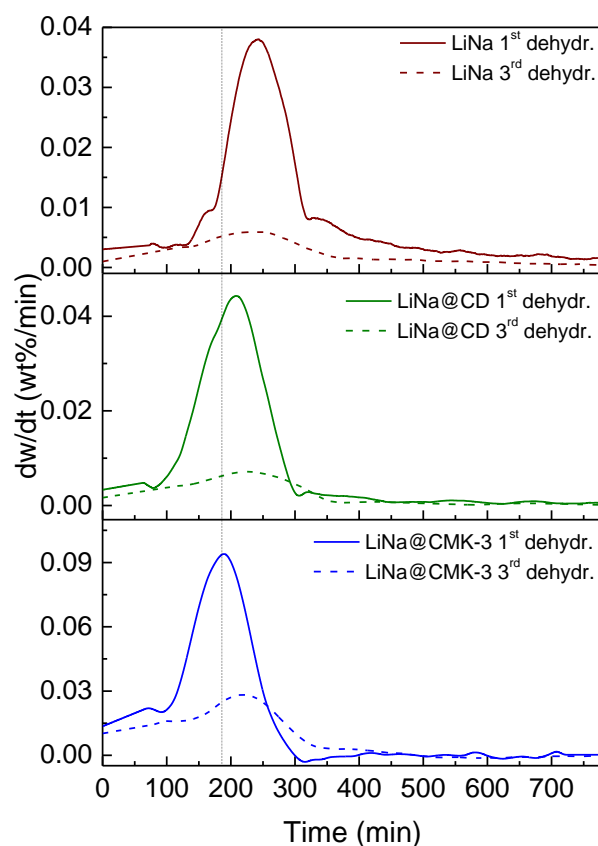


Figure 6. Derivative curves of the H_2 release versus time measured with a manometric device (Sieverts method, data shown in Figure 5) for LiNa (dark red), LiNa/CD (green) and LiNa/CMK-3 (blue).

3. Discussion

The XRPD pattern, as well as the SEM study of LiNa/CMK-3, suggest that although most of the borohydride particles were successfully introduced into the porous scaffold, a small part of the hydride material remained outside the pores. Nevertheless, the proof of an overall successful infiltration was provided by the pore network properties pre- and post infiltration as derived from the N_2 adsorption/desorption isotherms at 77 K (approx. -196 °C). The TPV of the CMK-3 was reduced from $1.2 \text{ cm}^3 \text{ g}^{-1}$ to $0.21 \text{ cm}^3 \text{ g}^{-1}$ with a loss of about the 82.5% of the pore volume. It should be noted that the volume of the composite borohydride (LiNa) used for the infiltration was 60% of the CMK-3 pore volume, and thus in principle a corresponding reduction of the pore volume was expected. This difference can be attributed to pore blocking caused by the molten phase in a way that some extra closed porosity (empty yet inaccessible to N_2 molecules) was created. A similar picture was obtained by examining the dramatic decrease in the BET area of the carbon, from 1250 m^2 to only $170 \text{ m}^2 \text{ g}^{-1}$ after the melt infiltration. This reduction was even more pronounced (86.5%) in accordance with the pore blocking mechanism. In brief, the blocking of smaller pores reduced the BET area more than the pore volume as the surface to volume ratio increased with decreasing pore size.

The TPD-MS experiments showed the H_2 release during the thermal decomposition, without detectable traces of undesired gases such as B_2H_6 (all the recorded m/z signals analyzed are reported in Section 4). The experimental results allowed us to resolve the multiple decomposition stages particularly evident in the bulk LiNa, from about 280 °C until the last main dehydrogenation occurring at about 490 °C. Additionally, the role of the carbons on the borohydrides' decomposition is highlighted by the TPD-MS results.

The presence of a high surface mesoporous carbon such as CMK-3 allowed the decomposition to take place at temperatures even 130 °C lower than the bulk hydride mixture, in accordance with previous observations for carbon aerogels [49]. The relative intensity of the two main dehydrogenation signals was maintained, suggesting that all the reactive components were affected by the carbon presence. On the other hand, the composite with the non-porous carbon (LiNa/CD) also showed lower decomposition temperatures, with the dehydrogenation events occurring in a range of temperatures between the bulk and the LiNa/CMK composite, suggesting an intermediate behavior. Contrary to what is generally believed, the decrease in the decomposition temperature suggests that even without nanoconfinement the carbon provided a kinetic improvement to the decomposition reaction. The inferior performance of LiNa/CD compared with LiNa/CMK may perhaps be explained by the significantly lower surface area of the CD substrate. Similar results were obtained by nanoconfinement of sodium aluminum hydride, NaAlH₄, in carbons with different pore sizes in the range 7 to 100 nm. A significant contribution to the observed improvements of kinetics and reversibility was assigned to the catalytic effects of the carbon scaffolds along with a minor contribution from the nanosizing, i.e., confinement in pores in the range of 7 to 39 nm [65].

A similar behavior was observed by the manometric study of the dehydrogenation/rehydrogenation of the samples. While the pure eutectic LiNa mixture decomposed at high temperatures and showed a non-reversible behavior, the carbon composites allowed lower decomposition temperatures and provided the system with some degree of reversibility. Especially for the case of LiNa/CMK-3, it can be seen that after the first two cycles the amount of hydrogen exchanged was constant, with a H₂ uptake of about 3.5 wt.%. The carbon discs had a comparable effect on LiNa; however, as expected due to the smaller surface area, the reversible hydrogen uptake was limited and did not exceed 1.5 wt.% of H₂. Unlike the kinetic enhancement that was attributed to the catalytic effect of the carbon surface, the stability of the system under cycling may be attributed to confinement since the pore network provided a space where extended aggregation was difficult. The reversible part of the LiNa/CD can, in this respect, be associated with the part of the molten phase that was directly “bound” to the surface of the CDs, thus hampering agglomeration.

From the study of the derivatives of the dehydrogenation curves it is possible to conclude that the decomposition of the carbon composites starts at lower temperatures than the bulk eutectic mixture. There is an obvious kinetic improvement for LiNa/CMK-3, which is less pronounced for LiNa/CD. However, this behavior is somehow limited to the first dehydrogenation cycles, and the kinetic enhancement is practically lost for the third cycle. This behavior may be related to the loss of the destabilizing interaction between the hydrides and the carbon surface after cycling. It is quite obvious from the integral curves that in all cases there is a major loss of activity between the first and second cycle, implying that at least a part of the material is dehydrogenated irreversibly in the bulk but also under confinement.

4. Materials and Methods

Sample preparation. The CMK-3 carbon scaffold was synthesized through nanocasting using SBA-15 porous silica (Claytec Inc., East Lansing, MI, USA) as hard template. In order to achieve an adequately narrow pore size distribution and a smaller mean pore size, a procedure slightly different from the one originally proposed by Ryoo et al. [51] was adopted; this approach involved three impregnation steps with the carbon precursor instead of just two [66], and allowed a very good control of the pore size of CMK-3, at the cost of a small reduction of the surface area and pore volume. More specifically, 1 g of dried SBA-15 powder was impregnated with 5 mL of an aqueous solution containing 1.25 g of sucrose (Merck, Darmstadt, Germany) as carbon precursor and 0.07 mL of sulfuric acid (Merck, Darmstadt, Germany) in order to promote the polymerization-caramelization reactions that were carried out in an oven. The sample was initially heated from room temperature to 100 °C with a heating rate of 10 °C min⁻¹. After 6 h at a constant temperature, the sample

was further heated up to 160 °C (10 °C min⁻¹) and left overnight. The whole procedure of impregnation with the sucrose solution and thermal treatment was then repeated two more times, while gradually reducing (by 65% each time) the solution concentration. In order to complete the carbonization process, the carbon–silica composite material was pyrolyzed in a tubular furnace (GSL 1100 X, MTI, CA, USA) at 900 °C under nitrogen flow. During this process, which lasted approx. 6 h, the residual hydrogen and oxygen were eliminated and the carbon structure was consolidated. The silica template was then dissolved by washing the composite material with a 40% solution of hydrofluoric acid. In order to completely remove the acidic solution from the porous carbon structure, the material was subjected to a series of centrifugations at 9000 RPM (Universal 320, Hettich, Tuttlingen, Germany) and water additions. The resulting CMK-3 type carbon was then washed and filtered under vacuum with water and ethanol and dried overnight in an oven at 100 °C. The mesoporous carbon obtained with this procedure may still have residual oxygen functional groups on the surface that may react and oxidize the borohydrides. For this reason, the as-produced CMK-3 was further treated in a tubular furnace at 700 °C under a stream of argon. This process removes the surface functional groups and may increase the amount of accessible micropores, thus increasing the material's total surface area [67]. The sample was stored at ambient conditions; however, before using it as a host for infiltrating borohydrides it was thoroughly outgassed overnight under high vacuum at 250 °C and consequently stored in an argon-filled glove box (LABstar, MBraun, Garching, Germany).

The non-porous carbon used (n-TEC, Norway) consisted of carbon discs (CD) made by multiple graphitic layers having an average thickness of 20–50 nm and diameter of about 0.8–3 µm. This type of carbon was synthesized through the pyrolysis of hydrocarbons using a plasma torch process. Similarly to the CMK-3 material, the CDs were also heat treated before use in a tubular furnace at 700 °C under inert atmosphere for about 3 h.

The eutectic mixture of the two borohydrides 0.71 LiBH₄–0.29 NaBH₄ (referred to as LiNa) was prepared according to the previously described procedures [49] using the eutectic molar ratio studied by Dematteis et al. [43]. The two pure salts, LiBH₄ (95%, Sigma-Aldrich, St. Louis, MO, USA) and NaBH₄ (97%, Sigma-Aldrich, St. Louis, MO, USA), were stored in an argon-filled glove box and mixed at a molar ratio 0.71:0.29, first manually with a pestle and mortar, and then mechano-chemically using a planetary ball mill (Pulverisette 4, Fritch GmbH, Idar-Oberstein, Germany). The powders were milled in a gas-tight tungsten carbide jar with internal volume of 80 mL, using tungsten carbide spheres with 10 mm diameter and a 1:30 powder to balls ratio. The total mixing time necessary to obtain a homogeneous mixture was about 1 h at 350 RPM. However, due to the low melting temperature of the LiNa mixture and in order to avoid unwanted reactions during the high energy process, processing was divided into 30 cycles of 2 min of milling followed by 2 min of pause, which was necessary to let the powders cool down to room temperature. In addition, the sample treatment as well as the ball milling reactor loading and unloading was performed under inert argon atmosphere, with H₂O and O₂ concentrations <0.5 ppm.

The low melting temperature of the obtained eutectic borohydride mixture allowed the filling of the CMK-3 carbon pores via melt infiltration. A calculated amount of LiNa with a volume equal to 60% of the total pore volume (TPV) of the carbon scaffold was used for the melt infiltration. Taking into account the total pore volume of the carbon (TPV = 1.2 cm³ g⁻¹) and the density of the eutectic mixture (0.78 g cm⁻³), the carbon and hydrides were mixed together with a mass ratio of CMK-3: LiNa equal to 1.76:1. All the handling processes necessary to obtain a homogeneous mixture of carbon and hydrides were performed in an argon-filled glove box. The manually mixed LiNa/CMK-3 composite was transferred to a high pressure stainless steel gas tight reactor under argon (1 atm). The reactor was then sealed, removed from the glove box and attached to a custom-made manometric apparatus, where the actual melt infiltration took place. After being meticulously outgassed, the system was loaded with an overpressure of ~100 bar of H₂ in order to avoid any unwanted dehydrogenation reactions during melt infiltration.

The sample in the reactor was heated up to 250 °C with a heating ramp of 3 °C min⁻¹ and the final temperature was kept constant for 30 min, allowing the infiltration of the molten hydride inside the carbon pores. The approach for CMK-3, LiNa and LiNa/CMK-3 preparation is schematically presented in Figure 7. The same procedure was also used for the synthesis of an “equivalent” composite material combining the LiNa mixture with the non-porous CDs (namely LiNa/CD), where nanoconfinement does not take place. In this case, since the carbon disks are non-porous, the carbon material and the hydrides were mixed with the same mass ratio used for the LiNa/CMK-3 composite, i.e., 1.76:1.

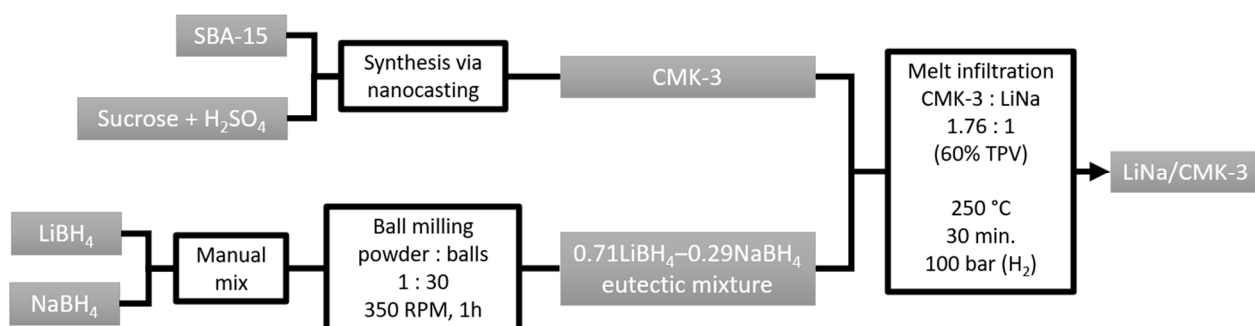


Figure 7. Schematic representation of the experimental procedure leading to the synthesis of the LiNa/CMK-3 composite.

Finally, for reference, the bulk LiNa was also heat treated at 250 °C for 30 min under 100 bar of H₂, simulating the infiltration process.

The efficiency of the infiltration of the eutectic mixture in the pores of the CMK-3 carbon was evaluated through a series of powder X-ray diffraction (XRPD) measurements, using a Rigaku RAXIS IV Imaging Plate Detector mounted on a Rigaku RU-H3R Rotating Copper Anode X-ray Generator ($\lambda = 1.54 \text{ \AA}$) and N₂ sorption measurements at 77 K, using a volumetric gas adsorption analyzer (Autosorb-1-MP, Quantachrome Instruments, Boynton Beach, FL, USA). High vacuum (10⁻⁶ mbar) was applied to the materials in order to outgas the samples before analysis. The specific surface area of the materials was calculated according to the Brunauer–Emmett–Teller (BET) method, employing the BET consistency criteria (ISO 9277:2010). The pore size distribution was calculated through the QSDFT (quenched solid density functional theory) method assuming slit/cylindrical pore models. The total pore volume was calculated at $p/p_0 = 0.98$. The morphology of the infiltrated scaffold was also examined on a JSM 7401F (JEOL Ltd., Akishima, Tokyo, Japan) field emission scanning electron microscope (SEM) using the Gentle Beam mode.

The thermal decomposition of both the bulk LiNa as well as the carbon-based composites was studied with temperature programmed desorption coupled with mass spectrometry (TPD/MS). The sample was contained in a quartz cell, part of a custom-made set-up, and was heated up using a furnace under a constant carrier gas stream (argon) regulated by a mass flow controller (80 mL min⁻¹). In a typical run, the sample was heated up to 700 °C with a heating ramp of 5 °C min⁻¹. The decomposition products were transferred with the aid of the carrier gas to an OmniStar GSD 301 O1 (Pfeiffer Vacuum Technology AGm Aßlar, Germany) quadrupole mass spectrometer and then vented. The temporal change of intensity at m/z : 2, 4, 15–18, 23–28, 32, 44, 79 and 80 was continuously recorded.

The absorption–desorption capacity of the materials under five dehydrogenation/hydrogenation cycles were investigated with a custom-made high pressure manometric device (Sieverts apparatus). The respective experiments involved a dehydrogenation step under an initial back-pressure of ~1.5 bar, during which the sample was heated up with a heating rate of 2 °C min⁻¹ from room temperature up to 450 °C, then the system was kept at this temperature for 10 h and consequently cooled down freely back to room temperature. The second part of the experiment involved the rehydrogenation of the sample, performed under an initial pressure of about 100 bar of hydrogen. The sample was heated up with a rate of 5 °C min⁻¹ from room temperature up to 450 °C. The high temperature was kept

constant for 12 h in order to allow the material to absorb as much hydrogen as possible before cooling down to room temperature. The dehydrogenation and hydrogenation procedure (Figure 8) were repeated 5 times for each sample.

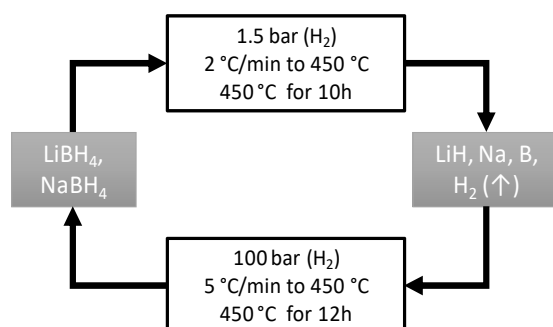


Figure 8. Schematic representation of the LiNa dehydrogenation/rehydrogenation process carried out with a custom-made Sievert apparatus. The amount of H₂ released by LiNa and LiNa composites was calculated after heating the material to 450 °C under 1.5 bar of H₂ pressure. The products were then re-hydrogenated at 450 °C under 100 bar of H₂ pressure. The cycle was repeated five times.

5. Conclusions

The low melting temperature of the 0.71 LiBH₄–0.29 NaBH₄ (LiNa) eutectic mixture allowed the nanoconfinement of the hydrides in the ~5 nm diameter pores of a CMK-3 type carbon, as well as the synthesis of a borohydride/non-porous carbon composite. For both the porous and non-porous carbon hosts an improvement on the hydrogen absorption-release properties over the bulk hydrides (LiNa) was observed. The carbon-LiNa composites revealed faster decomposition kinetics compared with bulk LiNa, while the effect is more obvious for the nanoconfined material. However, the kinetic improvements decrease with cycling. Moreover, the presence of carbon increased the reaction reversibility compared with the bulk material. The nanoconfined LiNa shows a consistent uptake of H₂ of about 3.5 wt.% after five hydrogenation/dehydrogenation cycles. A similar behavior but with minor intensity was revealed by the composite material with non-porous carbon, which can exchange about 1.5 wt.% of H₂ after five cycles. Both the kinetic improvement observed for the carbon composite materials and the reversibility are probably associated with surface catalytic interactions; confinement in porous materials with high surface area seems to amplify such effects, leading to overall better performance.

Author Contributions: Conceptualization, T.R.J., G.C. and T.S.; Methodology, F.P.; Investigation, F.P. and S.P.; Data curation, F.P.; Writing—original draft, F.P.; Writing—review & editing, T.R.J., G.C. and T.S.; Visualization, S.P.; Supervision, T.R.J., G.C. and T.S. All authors have read and agreed to the published version of the manuscript.

Funding: This research received funding from the European Marie Curie Actions under ECOSTORE grant agreement No. 607040. The work of F.P. was also partially supported by the H2020 project ENDURUNS (Grant agreement: 824348).

Data Availability Statement: The data presented in this study are available on request from the corresponding author.

Acknowledgments: F.P. would like to acknowledge P. Kyritsis and Ch.A. Mitsopoulou (Inorganic Chemistry Laboratory, Department of Chemistry of the National and Kapodistrian University of Athens, Greece) for the fruitful discussions and their support during the realization of this work.

Conflicts of Interest: The authors declare no conflict of interest.

References

1. Asghar, U.; Rafiq, S.; Anwar, A.; Iqbal, T.; Ahmed, A.; Jamil, F.; Khurram, M.S.; Akbar, M.M.; Farooq, A.; Shah, N.S.; et al. Review on the Progress in Emission Control Technologies for the Abatement of CO₂, SO_x and NO_x from Fuel Combustion. *J. Environ. Chem. Eng.* **2021**, *9*, 106064. [\[CrossRef\]](#)
2. Beringer, S.L. Energy, Climate Change and EU Development Policy. In *EU Development Policies*; Palgrave Macmillan: Cham, Switzerland, 2019; pp. 17–34. ISBN 9783030013073.
3. Zhou, Y.; Li, R.; Lv, Z.; Liu, J.; Zhou, H.; Xu, C. Green Hydrogen: A Promising Way to the Carbon-Free Society. *Chin. J. Chem. Eng.* **2022**, *43*, 2–13. [\[CrossRef\]](#)
4. Bongartz, D.; Dore', L.; Eichler, K.; Grube, T.; Heuser, B.; Hombach, L.E.; Robinius, M.; Pischinger, S.; Stolten, D.; Walther, G. Comparison of Light-Duty Transportation Fuels Produced from Renewable Hydrogen and Green Carbon Dioxide. *Appl. Energy* **2018**, *231*, 757–767. [\[CrossRef\]](#)
5. Abe, J.O.; Popoola, A.P.I.; Ajenifuja, E.; Popoola, O.M. Hydrogen Energy, Economy and Storage: Review and Recommendation. *Int. J. Hydrogen Energy* **2019**, *44*, 15072–15086. [\[CrossRef\]](#)
6. Ball, M.; Weeda, M. The Hydrogen Economy - Vision or Reality? *Int. J. Hydrogen Energy* **2015**, *40*, 7903–7919. [\[CrossRef\]](#)
7. Lai, Q.; Paskevicius, M.; Sheppard, D.A.; Buckley, C.E.; Thornton, A.W.; Hill, M.R.; Gu, Q.; Mao, J.; Huang, Z.; Liu, H.K.; et al. Hydrogen Storage Materials for Mobile and Stationary Applications: Current State of the Art. *ChemSusChem* **2015**, *8*, 2789–2825. [\[CrossRef\]](#) [\[PubMed\]](#)
8. Hua, T.Q.; Roh, H.S.; Ahluwalia, R.K. Performance Assessment of 700-Bar Compressed Hydrogen Storage for Light Duty Fuel Cell Vehicles. *Int. J. Hydrogen Energy* **2017**, *42*, 25121–25129. [\[CrossRef\]](#)
9. Zhang, J.; Yan, Y.; Zhang, C.; Xu, Z.; Li, X.; Zhao, G.; Ni, Z. Properties Improvement of Composite Layer of Cryo-Compressed Hydrogen Storage Vessel by Polyethylene Glycol Modified Epoxy Resin. *Int. J. Hydrogen Energy* **2022**, *48*, 5576–5594. [\[CrossRef\]](#)
10. Zhao, X.; Yan, Y.; Zhang, J.; Zhang, F.; Wang, Z.; Ni, Z. Analysis of Multilayered Carbon Fiber Winding of Cryo-Compressed Hydrogen Storage Vessel. *Int. J. Hydrogen Energy* **2022**, *47*, 10934–10946. [\[CrossRef\]](#)
11. Rivard, E.; Trudeau, M.; Zaghbi, K. Hydrogen Storage for Mobility: A Review. *Materials* **2019**, *12*, 1973. [\[CrossRef\]](#)
12. Balasooriya, W.; Clute, C.; Schritteser, B.; Pinter, G. A Review on Applicability, Limitations, and Improvements of Polymeric Materials in High-Pressure Hydrogen Gas Atmospheres. *Polym. Rev.* **2022**, *62*, 175–209. [\[CrossRef\]](#)
13. Grinderslev, J.B.; Amdisen, M.B.; Skov, L.N.; Møller, K.T.; Kristensen, L.G.; Polanski, M.; Heere, M.; Jensen, T.R. New Perspectives of Functional Metal Borohydrides. *J. Alloys Compd.* **2022**, *896*, 163014. [\[CrossRef\]](#)
14. Schneemann, A.; White, J.L.; Kang, S.; Jeong, S.; Wan, L.F.; Cho, E.S.; Heo, T.W.; Prendergast, D.; Urban, J.; Wood, B.C.; et al. Nanostructured Metal Hydrides for Hydrogen Storage. *Chem. Rev.* **2018**, *118*, 10775–10839. [\[CrossRef\]](#)
15. Hadjixenophontos, E.; Dematteis, E.M.; Berti, N.; Wołczyk, A.R.; Huen, P.; Brighi, M.; Le, T.T.; Santoru, A.; Payandeh, S.H.; Peru, F.; et al. A Review of the MSCA ITN ECOSTORE—Novel Complex Metal Hydrides for Efficient and Compact Storage of Renewable Energy as Hydrogen and Electricity. *Inorganics* **2020**, *8*, 17. [\[CrossRef\]](#)
16. Hirscher, M.; Yartys, V.A.; Baricco, M.; Bellosta von Colbe, J.; Blanchard, D.; Bowman, R.C.J.; Broom, D.P.; Buckley, C.E.; Chang, F.; Chen, P.; et al. Materials for Hydrogen-Based Energy Storage—Past, Recent Progress and Future Outlook. *J. Alloys Compd.* **2020**, *827*, 153548. [\[CrossRef\]](#)
17. Dematteis, E.M.; Amdisen, M.B.; Autrey, T.; Barale, J.; Bowden, M.E.; Buckley, C.E.; Cho, Y.W.; Deledda, S.; Dornheim, M.; De Jongh, P.; et al. Hydrogen Storage in Complex Hydrides: Past Activities and New Trends. *Prog. Energy* **2022**, *4*, 032009. [\[CrossRef\]](#)
18. Eghbali, P.; Nişanlı, B.; Metin, Ö. Graphene Hydrogel Supported Palladium Nanoparticles as an Efficient and Reusable Heterogeneous Catalysts in the Transfer Hydrogenation of Nitroarenes Using Ammonia Borane as a Hydrogen Source. *Pure Appl. Chem.* **2018**, *90*, 327–335. [\[CrossRef\]](#)
19. Eghbali, P.; Gürbüz, M.U.; Ertürk, A.S.; Metin, Ö. In Situ Synthesis of Dendrimer-Encapsulated palladium(0) Nanoparticles as Catalysts for Hydrogen Production from the Methanolysis of Ammonia Borane. *Int. J. Hydrogen Energy* **2020**, *45*, 26274–26285. [\[CrossRef\]](#)
20. Bellosta von Colbe, J.; Ares, J.R.; Barale, J.; Baricco, M.; Buckley, C.; Capurso, G.; Gallandat, N.; Grant, D.M.; Guzik, M.N.; Jacob, I.; et al. Application of Hydrides in Hydrogen Storage and Compression: Achievements, Outlook and Perspectives. *Int. J. Hydrogen Energy* **2019**, *44*, 7780–7808. [\[CrossRef\]](#)
21. Manickam, K.; Mistry, P.; Walker, G.; Grant, D.; Buckley, C.E.; Humphries, T.D.; Paskevicius, M.; Jensen, T.; Albert, R.; Peinecke, K.; et al. Future Perspectives of Thermal Energy Storage with Metal Hydrides. *Int. J. Hydrogen Energy* **2019**, *44*, 7738–7745. [\[CrossRef\]](#)
22. Mazzucco, A.; Dornheim, M.; Sloth, M.; Jensen, T.R.; Oluf, J.; Rokni, M. Bed Geometries, Fueling Strategies and Optimization of Heat Exchanger Designs in Metal Hydride Storage Systems for Automotive Applications: A Review. *Int. J. Hydrogen Energy* **2014**, *39*, 17054–17074. [\[CrossRef\]](#)
23. Yartys, V.A.; Lototskyy, M.V.; Akiba, E.; Albert, R.; Antonov, V.E.; Ares, J.R.; Baricco, M.; Bourgeois, N.; Buckley, C.E.; Bellosta von Colbe, J.M.; et al. Magnesium Based Materials for Hydrogen Based Energy Storage: Past, Present and Future. *Int. J. Hydrogen Energy* **2019**, *44*, 7809–7859. [\[CrossRef\]](#)
24. Callini, E.; Aguey-Zinsou, K.F.; Ahuja, R.; Ares, J.R.; Bals, S.; Biliškov, N.; Chakraborty, S.; Charalambopoulou, G.; Chaudhary, A.L.; Cuevas, F.; et al. Nanostructured Materials for Solid-State Hydrogen Storage: A Review of the Achievement of COST Action MP1103. *Int. J. Hydrogen Energy* **2016**, *41*, 14404–14428. [\[CrossRef\]](#)

25. Møller, K.T.; Jensen, T.R.; Akiba, E.; Li, H. Hydrogen - A Sustainable Energy Carrier. *Prog. Nat. Sci. Mater. Int.* **2017**, *27*, 34–40. [[CrossRef](#)]
26. Puzkiel, J.; Gasnier, A.; Amica, G.; Gennari, F. Tuning LiBH_4 for Hydrogen Storage: Destabilization, Additive, and Nanoconfinement Approaches. *Molecules* **2020**, *25*, 163. [[CrossRef](#)]
27. Demirci, U.B.; Miele, P. Sodium Borohydride versus Ammonia Borane, in Hydrogen Storage and Direct Fuel Cell Applications. *Energy Environ. Sci.* **2009**, *2*, 627–637. [[CrossRef](#)]
28. Møller, K.T.; Sheppard, D.; Ravnsbæk, D.B.; Buckley, C.E.; Akiba, E.; Li, H.; Jensen, T.R. Complex Metal Hydrides for Hydrogen, Thermal and Electrochemical Energy Storage. *Energies* **2017**, *10*, 1645. [[CrossRef](#)]
29. Lai, Q.; Aguey-Zinsou, K.-F.; Lai, Q.; Aguey-Zinsou, K.-F. Borohydrides as Solid-State Hydrogen Storage Materials: Past, Current Approaches and Future Perspectives. *Gen. Chem.* **2018**, *4*, 180017. [[CrossRef](#)]
30. Milanese, C.; Jensen, T.R.; Hauback, B.C.; Pistidda, C.; Dornheim, M.; Yang, H.; Lombardo, L.; Zuetzel, A.; Filinchuk, Y.; Ngene, P.; et al. Complex Hydrides for Energy Storage. *Int. J. Hydrogen Energy* **2019**, *44*, 7860–7874. [[CrossRef](#)]
31. Paskevicius, M.; Jepsen, L.H.; Schouwink, P.; Černý, R.; Ravnsbæk, D.B.; Filinchuk, Y.; Dornheim, M.; Besenbacher, F.; Jensen, T.R. Metal Borohydrides and Derivatives-Synthesis, Structure and Properties. *Chem. Soc. Rev.* **2017**, *46*, 1565–1634. [[CrossRef](#)]
32. Callini, E.; Özlem Kocabas Atakli, Z.; Hauback, B.C.; Orimo, S.-I.; Jensen, C.; Dornheim, M.; Grant, D.; Cho, Y.W.; Chen, P.; Hjörvarsson, B.; et al. Complex and Liquid Hydrides for Energy Storage. *Appl. Phys. A* **2016**, *122*, 353. [[CrossRef](#)]
33. Javadian, P.; Payandeh, S.G.; Sheppard, D.A.; Buckley, C.E.; Jensen, T.R. Reversibility of LiBH_4 Facilitated by the $\text{LiBH}_4\text{-Ca}(\text{BH}_4)_2$ Eutectic. *J. Phys. Chem. C* **2017**, *121*, 18439–18449. [[CrossRef](#)]
34. Černý, R.; Murgia, F.; Brighi, M. Metal Hydroborates: From Hydrogen Stores to Solid Electrolytes. *J. Alloys Compd.* **2022**, *895*, 162659. [[CrossRef](#)]
35. Paskevicius, M.; Ley, M.B.; Sheppard, D.A.; Jensen, T.R.; Buckley, C.E. Eutectic Melting in Metal Borohydrides. *Phys. Chem. Chem. Phys.* **2013**, *15*, 19774–19789. [[CrossRef](#)] [[PubMed](#)]
36. Nakamori, Y.; Orimo, S.I. Destabilization of Li-Based Complex Hydrides. *J. Alloys Compd.* **2004**, *370*, 271–275. [[CrossRef](#)]
37. Nickels, E.A.; Jones, M.O.; David, W.I.F.; Johnson, S.R.; Lowton, R.L.; Sommariva, M.; Edwards, P.P. Tuning the Decomposition Temperature in Complex Hydrides: Synthesis of a Mixed Alkali Metal Borohydride. *Angew. Chemie Int. Ed.* **2008**, *47*, 2817–2819. [[CrossRef](#)] [[PubMed](#)]
38. Shao, J.; Xiao, X.; Fan, X.; Huang, X.; Zhai, B.; Li, S.; Ge, H.; Wang, Q.; Chen, L. Enhanced Hydrogen Storage Capacity and Reversibility of LiBH_4 Nanoconfined in the Densified Zeolite-Templated Carbon with High Mechanical Stability. *Nano Energy* **2015**, *15*, 244–255. [[CrossRef](#)]
39. Zhang, L.; Zheng, J.; Xiao, X.; Fan, X.; Huang, X.; Yang, X.; Chen, L. Enhanced Hydrogen Storage Properties of a Dual-Cation (Li^+ , Mg^{2+}) Borohydride and Its Dehydrogenation Mechanism. *RSC Adv.* **2017**, *7*, 36852–36859. [[CrossRef](#)]
40. Zhang, L.; Zheng, J.; Chen, L.; Xiao, X.; Qin, T.; Jiang, Y.; Li, S.; Ge, H.; Wang, Q. Remarkable Enhancement in Dehydrogenation Properties of $\text{Mg}(\text{BH}_4)_2$ Modified by the Synergetic Effect of Fluorographite and LiBH_4 . *Int. J. Hydrogen Energy* **2015**, *40*, 14163–14172. [[CrossRef](#)]
41. El Kharbachi, A.; Pinatel, E.; Nuta, I.; Baricco, M. A Thermodynamic Assessment of LiBH_4 . *Calphad Comput. Coupling Phase Diagrams Thermochem.* **2012**, *39*, 80–90. [[CrossRef](#)]
42. Urganli, J.; Torres, F.J.; Palumbo, M.; Baricco, M. Hydrogen Release from Solid State NaBH_4 . *Int. J. Hydrogen Energy* **2008**, *33*, 3111–3115. [[CrossRef](#)]
43. Dematteis, E.M.; Roedern, E.; Pinatel, E.R.; Corno, M.; Jensen, T.R.; Baricco, M. A Thermodynamic Investigation of the $\text{LiBH}_4\text{-NaBH}_4$ System. *RSC Adv.* **2016**, *6*, 60101–60108. [[CrossRef](#)]
44. Plerdsranoy, P.; Kaewsuan, D. Effects of Specific Surface Area and Pore Volume of Activated Carbon Nanofibers on Nanoconfinement and Dehydrogenation of LiBH_4 . *Int. J. Hydrogen Energy* **2017**, *42*, 6189–6201. [[CrossRef](#)]
45. Sofianos, M.V.; Chaudhary, A.; Paskevicius, M.; Sheppard, D.A.; Humphries, T.D.; Dornheim, M.; Buckley, C.E. Hydrogen Storage Properties of Eutectic Metal Borohydrides Melt-Infiltrated into Porous Al Scaffolds. *J. Alloys Compd.* **2019**, *775*, 474–480. [[CrossRef](#)]
46. Suryanarayana, C. Mechanical Alloying and Milling. *Prog. Mater. Sci.* **2001**, *46*, 1–184. [[CrossRef](#)]
47. Le Caër, G.; Delcroix, P.; Bégin-Colin, S.; Ziller, T. High-Energy Ball-Milling of Alloys and Compounds. *Hyperfine Interact.* **2002**, *141–142*, 63–72. [[CrossRef](#)]
48. Wu, C.; Cheng, H.M. Effects of Carbon on Hydrogen Storage Performances of Hydrides. *J. Mater. Chem.* **2010**, *20*, 5390–5400. [[CrossRef](#)]
49. Javadian, P.; Sheppard, D.A.; Buckley, C.E.; Jensen, T.R. Hydrogen Storage Properties of Nanoconfined $\text{LiBH}_4\text{-NaBH}_4$. *Int. J. Hydrogen Energy* **2015**, *40*, 14916–14924. [[CrossRef](#)]
50. Adams, R.M. Preparation of Diborane. *Adv. Chem.* **1961**, *32*, 60–68. [[CrossRef](#)]
51. Jun, S.; Joo, S.H.; Ryoo, R.; Kruk, M. Synthesis of New, Nanoporous Carbon with Hexagonally Ordered Mesoporous Structure. *J. Am. Chem. Soc.* **2000**, *122*, 10712–10713. [[CrossRef](#)]
52. Thommes, M.; Kaneko, K.; Neimark, A.V.; Olivier, J.P.; Rodriguez-Reinoso, F.; Rouquerol, J.; Sing, K.S.W. Physisorption of Gases, with Special Reference to the Evaluation of Surface Area and Pore Size Distribution (IUPAC Technical Report). *Pure Appl. Chem.* **2015**, *87*, 1051–1069. [[CrossRef](#)]

53. Liu, Y.; Reed, D.; Paterakis, C.; Contreras, L.; Baricco, M.; Book, D. Study of the Decomposition of a 0.62LiBH₄–0.38NaBH₄ Mixture. *Int. J. Hydrogen Energy* **2017**, *42*, 22480–22488. [[CrossRef](#)]
54. Orimo, S.; Nakamori, Y.; Eliseo, J.R.; Züttel, A.; Jensen, C.M. Complex Hydrides for Hydrogen Storage. *Chem. Rev.* **2007**, *107*, 4111–4132. [[CrossRef](#)] [[PubMed](#)]
55. Züttel, A.; Wenger, P.; Rentsch, S.; Sudan, P.; Mauron, P.; Emmenegger, C. LiBH₄ a New Hydrogen Storage Material. *J. Power Sources* **2003**, *118*, 1–7. [[CrossRef](#)]
56. Züttel, A.; Rentsch, S.; Fischer, P.; Wenger, P.; Sudan, P.; Mauron, P.; Emmenegger, C. Hydrogen Storage Properties of LiBH₄. *J. Alloys Compd.* **2003**, *356–357*, 515–520. [[CrossRef](#)]
57. Humphries, T.D.; Kalantzopoulos, G.N.; Llamas-Jansa, I.; Olsen, J.E.; Hauback, B.C. Reversible Hydrogenation Studies of NaBH₄ Milled with Ni-Containing Additives. *J. Phys. Chem. C* **2013**, *117*, 6060–6065. [[CrossRef](#)]
58. Mao, J.; Gregory, D.H. Recent Advances in the Use of Sodium Borohydride as a Solid State Hydrogen Store. *Energies* **2015**, *8*, 430–453. [[CrossRef](#)]
59. Orłowski, P.A.; Grochala, W. Effect of Vanadium Catalysts on Hydrogen Evolution from NaBH₄. *Solids* **2022**, *3*, 21. [[CrossRef](#)]
60. Mao, J.; Guo, Z.; Nevirkovets, I.P.; Liu, H.K.; Dou, S.X. Hydrogen De-/absorption Improvement of NaBH₄ Catalyzed by Titanium-Based Additives. *J. Phys. Chem. C* **2012**, *116*, 1596–1604. [[CrossRef](#)]
61. Orimo, S.I.; Nakamori, Y.; Ohba, N.; Miwa, K.; Aoki, M.; Towata, S.I.; Züttel, A. Experimental Studies on Intermediate Compound of LiBH₄. *Appl. Phys. Lett.* **2006**, *89*, 87–90. [[CrossRef](#)]
62. Reed, D.; Book, D. In-Situ Raman Study of the Thermal Decomposition of LiBH₄. *Mater. Res. Soc. Symp. Proc.* **2010**, *1216*, 2–8. [[CrossRef](#)]
63. Jensen, S.R.H.; Paskevicius, M.; Hansen, B.R.S.; Jakobsen, A.S.; Møller, K.T.; White, J.L.; Allendorf, M.D.; Stavila, V.; Skibsted, J.; Jensen, T.R. Hydrogenation Properties of Lithium and Sodium Hydride - Closo-Borate, [B₁₀H₁₀]²⁻ and [B₁₂H₁₂]²⁻, Composites. *Phys. Chem. Chem. Phys.* **2018**, *20*, 16266–16275. [[CrossRef](#)]
64. Ampoumogli, A.; Steriotis, T.; Trikalitis, P.; Giasafaki, D.; Bardaji, E.G.; Fichtner, M.; Charalambopoulou, G. Nanostructured Composites of Mesoporous Carbons and Boranates as Hydrogen Storage Materials. *J. Alloys Compd.* **2011**, *509*, S705–S708. [[CrossRef](#)]
65. Nielsen, T.K.; Javadian, P.; Polanski, M.; Besenbacher, F.; Bystrzycki, J.; Jensen, T.R. Nanoconfined NaAlH₄: Determination of Distinct Proliferative Effects from Pore Size, Crystallite Size, and Surface Interactions. *J. Phys. Chem. C* **2012**, *116*, 21046–21051. [[CrossRef](#)]
66. Peru, F.; Payandeh, S.; Charalambopoulou, G.; Jensen, T.R.; Steriotis, T. Hydrogen Sorption and Reversibility of the LiBH₄–KBH₄ Eutectic System Confined in a CMK-3 Type Carbon via Melt Infiltration. *J. Carbon Res.* **2020**, *2*, 19. [[CrossRef](#)]
67. Ampoumogli, A.; Charalambopoulou, G.; Javadian, P.; Richter, B.; Jensen, T.R.; Steriotis, T. Hydrogen Desorption and Cycling Properties of Composites Based on Mesoporous Carbons and a LiBH₄–Ca(BH₄)₂ Eutectic Mixture. *J. Alloys Compd.* **2015**, *645*, S480–S484. [[CrossRef](#)]

Disclaimer/Publisher's Note: The statements, opinions and data contained in all publications are solely those of the individual author(s) and contributor(s) and not of MDPI and/or the editor(s). MDPI and/or the editor(s) disclaim responsibility for any injury to people or property resulting from any ideas, methods, instructions or products referred to in the content.